DTU Library

Versatile high energy X-ray transparent electrolysis cell for operando measurements

Moss, Asger B.; Hätinen, Joel; Kúš, Peter; Garg, Sahil; Mirolo, Marta; Chorkendorff, Ib; Seger, Brian; Drnec, Jakub

Link back to DTU Orbit

Versatile high energy X-ray transparent electrolysis cell for *operando* measurements

Asger B. Moss[a], Joel Hätinen[b, c], Peter Kúš[d], Sahil Garg[a], Marta Mirolo[b], Ib Chorkendorff[a], Brian Seger[a], Jakub Drnec[b, *]

[a]*Surface Physics and Catalysis (SurfCat) Section, Department of Physics, Technical University of Denmark, 2800 Kgs. Lyngby, Denmark*

[b]*Experimental Division, European Synchrotron Radiation Facility, Grenoble, France*

[c]*Helsinki Institute of Physics, P.O. Box 64, FI-00014 University of Helsinki, Finland*

[d]*Department of Surface and Plasma Science, Faculty of Mathematics and Physics, Charles University, V Holešovičkách 2, 180 00 Prague 8, Czech Republic*

*Corresponding author: Jakub Drnec, Email: drnec@esrf.fr

Abstract

Herein we present a design for a versatile electrochemical cell for High Energy X-ray operando studies of Membrane Electrode Assembly (MEA) based electrochemical systems. The cell flowplate materials can be interchanged according to the needs of experiments, allowing studies of different chemistries and reactions. The design also allows for coupling the X-ray elastic scattering techniques with computed tomography reconstruction, opening the possibility of 3D mapping of chemical and structural properties in operating devices. The cell has originally been designed and tested for CO_2 electrolysis performance studies using Wide Angle X-ray Scattering (WAXS) technique.

1. Introduction

In the quest for a fossil fuel-free world, electrification has become a cornerstone in the strategy, and electrolysis appears to be a promising route for energy storage and renewable feedstock of chemicals[1]. So far, most research has been in the field of water electrolysis[2], but lately, the electrolysis of more complex reactions, such as CO_2 reduction reaction (CO_2RR[1,3]), has gained interest. In both water electrolysis and especially in CO_2 (and CO) electrolysis (CO_2E) one of the most promising cell designs is the zero-gap membrane electrode assembly (MEA) due to a low operating potential and simple configuration[4–6]. From a research perspective, the MEA does come with challenges. MEAs are inherently difficult to study *in situ* and operando conditions, and even *post mortem* analysis is relatively difficult as the assembly often suffers from mechanical instability when disassembled. With X-rays it is possible to investigate the MEA (during electrolysis operation) in grazing incidence geometry where the beam is parallel to the catalyst surface, but this requires a micro-sized beam at high energy and flux. With the development of 4th Generation synchrotrons, such as the European Synchrotron Radiation Facility Extremely Brilliant Source (ESRF-EBS), it is possible to obtain a beam suitable for such grazing incidence operando measurements. Grazing incidence measurements not only give a much larger interaction volume compared to the situation where the beam is perpendicular to the catalyst layer, but they also provide the possibility to investigate different MEA depths, i.e. anode and cathode GDEs, membrane, thin catalyst layer, etc. by moving the cell in the beam through a scanning method as illustrated in Figure *1*. However, the typical MEA cell cannot be used for X-ray operando experiments in this geometry, as this sets certain requirements regarding the cell shape and materials. Even though there exists many cells for X-ray experiments[7], most of them are not suitable for investigating MEAs for water splitting and CO_2 reduction experiments. Typically they are either significantly smaller than the typical cell, very challenging to assemble, or designed for use with the beam perpendicular to the GDE[8]. Therefore, this work aimed at designing a cell that

is both easy to work with, suitable for multiple applications and that can be used for a large variety of X-ray techniques, including Wide/Small Angle X-ray Scattering (W/SAXS), diffraction and absorption tomography, X-ray dark-field microscopy and possibly even coherent scattering experiments using high energy X-ray probe. While the cell can be used in many applications, in the following we will focus on the performance towards CO_2E to discuss the cell capabilities.
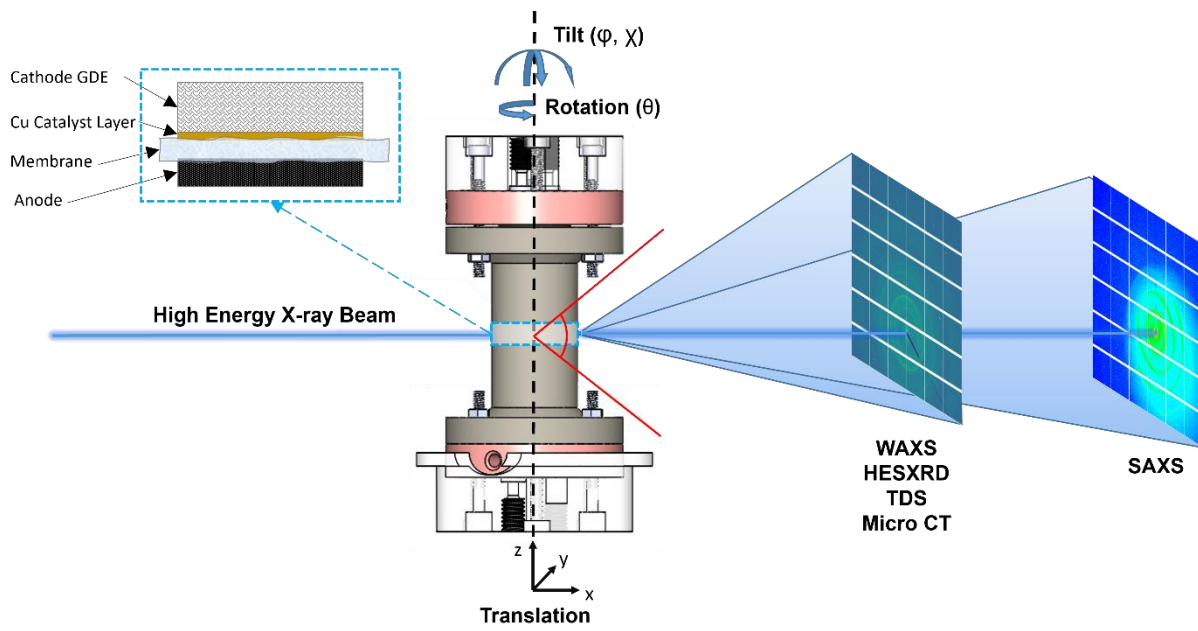
Figure 1. Illustration of the cell in the beam path. The magnification in the top left corner shows the placement and orientation of the Membrane Electrode Assembly (MEA). The cell can be moved in the beam (through translation and tilting) allowing for the different parts of the MEA to be investigated. The cell design allows X-rays scattered in wide angles (up to 30°) to exit unhindered as illustrated by the red lines. The circular design and the possibility to rotate it freely also enables the cell to be used for absorption and scattering tomography experiments.

2. Result and Discussion
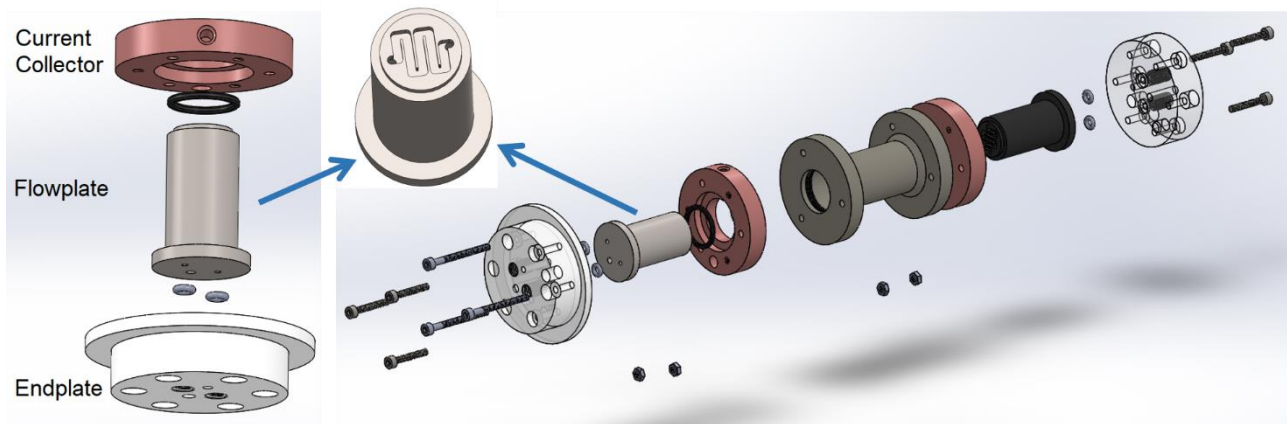
Figure 2. Left: Exploded view of the anode flowfield. Right: Exploded view of the whole cell. The insert shows the flowplate with the single-channel serpentine.

2.1. Cell design

The cell consists of three main parts; an anode flowfield, a cathode flowfield, and a polyether-ether ketone (PEEK) casing in which the two flowfields are inserted from each end (Figure *2*). Each flowfield consists of a 3D printed endplate in which the gas/liquid tubes are connected, a flowplate[†] of suitable material, e.g. graphite, Ti, or stainless steel, as well as anodic and cathodic current collectors, which also serve the purpose of fastening the flowplate to the endplate.

Unlike the typical MEA electrolyzer, the cell has a dog bone shape, with the MEA being placed in the middle. The design is chosen in order to have a wide opening without any blockage of the scattered X-rays making it possible to measure very wide angles and thereby a large portion of the reciprocal space. This is indicated by the red line in Figure 1. The circular design was chosen to enhance

---

[†] To avoid confusion the term flowplate is used for the raw piece, whereas the assembly of the endplate, flowplate and current collector is called flowfield.

tomography capabilities by minimizing potential reconstruction defects. Sealing between the flowfield and the membrane is ensured by a Viton O-ring which is slightly lowered into the flowfield. As the O-rings in the two flowfields are not fully submerged, a gap is created when the two flowfields are pushed together. This gap ensures that the GDEs are not compressed too much, e.g. so it loses its porosity or the cell short circuits.

The inner diameter of the O-ring is 9 mm leaving room for a disk-shaped GDE with a 63.6 mm^2 area. The diameter of the cell is small enough to allow for high-energy X-ray imaging, scattering, and tomography experiments with sufficient contrast and resolution and with minimal issues related to secondary scattering, parallax effect and absorption. At the same time, the electrode area is still of a size comparable to most experimental work in the CO_2E and water electrolysis fields thus allowing investigations that are relevant to commercial devices.

In order to obtain the dog bone shape, the flowplates are shaped as rods with a collar for fixation and a pin for alignment in one end and channels going through to the other end where a serpentine flow channel ensures gas or liquid transfer to the GDE. The flow channel geometry was chosen in this case to be a single channel serpentine with relatively wide channel dimensions. Though the geometry of the flow path is known to be important in electrolysis devices[9], a simple design was chosen both to minimize blockage from any salt deposition that may occur on the gas fed side of the device and to enhance bubble removal. This design also allows for unhindered X-ray analysis of the part of the GDE that might bulge into the serpentine. The channels are 1 mm deep, 1.25 mm wide, and 5.6 mm long and the lands are 0.25 mm. The exact geometry can be seen in the insert of Fig. 1. The flowfield assembly is designed in a way that allows easy flowplate exchange, so the flowplate can be manufactured from different materials and with different channel geometry.

The current collector is a Cu ring with a chamfer fitting the collar of the flowplate such that when assembled they form a flush surface towards the endplate. A hole in the side of the current collector can be used to connect to a potentiostat. The flowplate and current collector are firmly attached to the endplate by three screws that go through the endplate into the threads in the current collector. Two alignment pins ensure that the three parts are fixed and that the gas/liquid channels are placed correctly. Two small O-rings slightly submerged into the endplate creates a sealed connection and press the collar of the flowplate towards the current collector to ensure a good electrical connection.

Our initial design used metal quick connectors for the connection of gas and electrolyte tubes into the flowfields, but initial tests of CO_2E with a silver catalyst indicated a rapidly increasing H_2 selectivity with time. While the CO_2RR selectivity could be regained temporarily by a nitric acid wash of the cell, the following experiments always resulted in a similar performance loss. It is believed this H_2 selectivity increase was related to contamination from the metal quick connectors (most likely from Ni coming off the steel). The metal inlets were exchanged with 1/16" PTFE tubes inserted through the endplate. Further tests did not show the rapid increase in H_2 selectivity, thus this replacement resolved the contamination issue. A pressure-tight sealing was made using IDEX SuperFlangeless flat bottom ferrules (M-644-03, M-650). The inlet tube is extended beyond the ferrule and partially into the o-rings, thus sealing the side towards the flowplate. This sealing avoids the gas/liquid contacting the endplate or any metal part except the flowplate itself.

We expect the overall cell design to be capable of working under both highly acidic as well as alkaline conditions, since all gaskets can be exchanged depending on the specific use, and similarly the flowplates can be manufactured in a large variety of materials, with good electrical conductivity being the only general requirement. It should be noted that only neutral and moderately alkaline conditions were tested in this work.

2.2. Assembly

Due to the long casing, assembling the cell has substantial complexities. When assembling the cell, the membrane is first inserted slightly into the casing and then pushed all the way in using the flowplate with the GDE placed on top. In order to stabilize the membrane upon insertion, we used a 200 µm thick gasket (3-D printed from Stratasys VeroClear RGD810) that is placed on the anode side as the membrane otherwise tends to stick to the side when inserted. The gasket eases the assembly significantly and allows relatively consistent results. We have successfully tested PTFE, PFA, and FEP gaskets of similar dimensions. When fully inserted, the flowplate is tightened flush to the casing. This ensures that the height of the MEA is always the same making further alignment easier. The cell is then rotated 180 degrees so the cathode flowfield can be inserted with the cathode GDE lying on the top. The compression of the MEA is controlled by the tightening of the cathode flowfield to the casing.
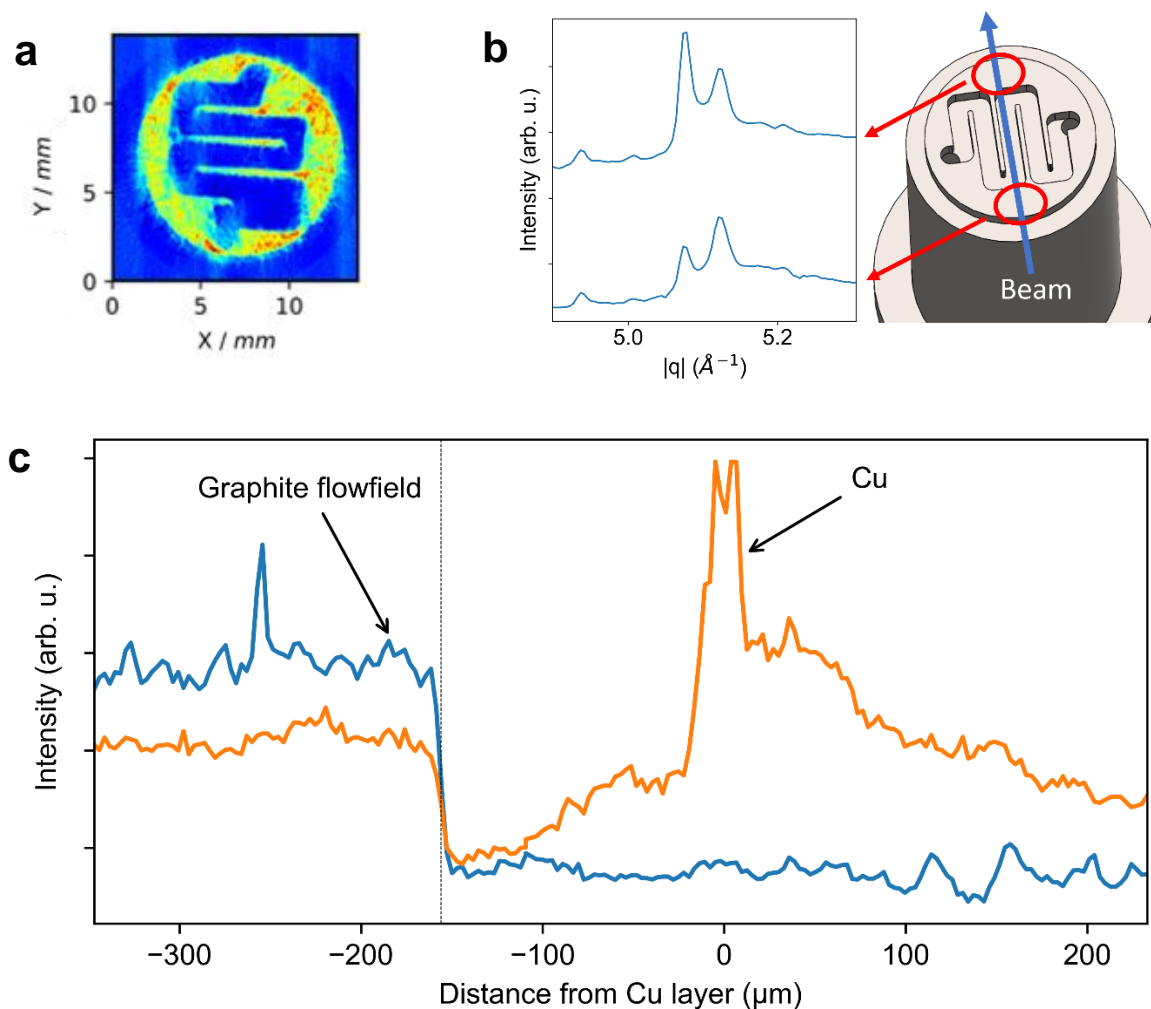
Figure 3. a) An example of an XRD-CT measurement taken at the height of the graphite flowfield. b) Example of a peak split from the graphite flowplate. The split comes when the beam diffracts on the two outer edges of the serpentine (reds circles), as these are distanced differently from the detector, and c) an example of how the surface of the land in the flow channel can be used to align the cell. The steeper the step in the graphite intensity is at -145 (dotted line), the more parallel is the cell and the beam. The orange line shows the Cu content indicating the height of the catalyst layer.

2.3. Alignment

The alignment of the cell for the grazing incident measurements is important in order to be able to investigate the different layers of the MEA correctly. The cell is mounted in a 6-axis alignment stage

8

so it can be moved, tilted and turned freely in all directions (x, y, z, θ, φ, χ), and thereby be aligned so the MEA is parallel to the beam. By using the polished land surface of the flowplate channels, it is possible to slowly tilt the cell, while scanning the height of the cell, until the signal from the surface of the land shows the steepest step function as shown by the example in Figure 3c. In order to minimize this iterative procedure, we have equipped the anode endplate with an edge fitting down in the holder. Thus the cell can be reproducibly mounted on the sample stage, giving a rough initial alignment of the cell.

2.4. Examples of data from an operando experiment

In a 2.5 h operando experiment, the cell was used for CO_2 electrolysis while WAXS scans were continuously acquired at various heights of the GDE by translating the cell in vertical direction. In this case, the line scan consisted of 50 different positions with a step size of 3 µm, and each line scan took around 100 s. In this way, we were able to obtain information on what happens inside the GDE (for more details, refer to Moss et al.[10]). Figure 4 shows 6 examples of WAXS patterns obtained at different positions in the beginning and toward the end of the experiment. The three patterns in Figure 4c are obtained at the height of the 150 nm thick catalyst layer and in all cases, clear peaks from the Cu catalyst can be seen. In the initial pattern obtained before the potential was applied peaks from both Cu and Cu_2O can be found, but after a very short time, the oxide phase disappears and the pattern does not change much from the beginning to the end of the experiment. This shows that the cell can be used to identify and follow the development of the crystalline phases of even a thin catalyst layer. Figure 4a and Figure 4b show patterns obtained approximately 90 µm and 45 µm from the catalyst layer towards the cathode flowfield. In both cases, a clear increase of the background at low q can be observed, which can be attributed to flooding of the GDE. In Figure 4a, the pattern obtained at the end of the experiments also shows the presence of a $KHCO_3$ phase caused by salt formations in the outer layers of the GDE. In total, it demonstrates how the cell can be used in operando experiments

to obtain important information not only on potential variations of the catalyst layer, but also of changes in the GDEs.
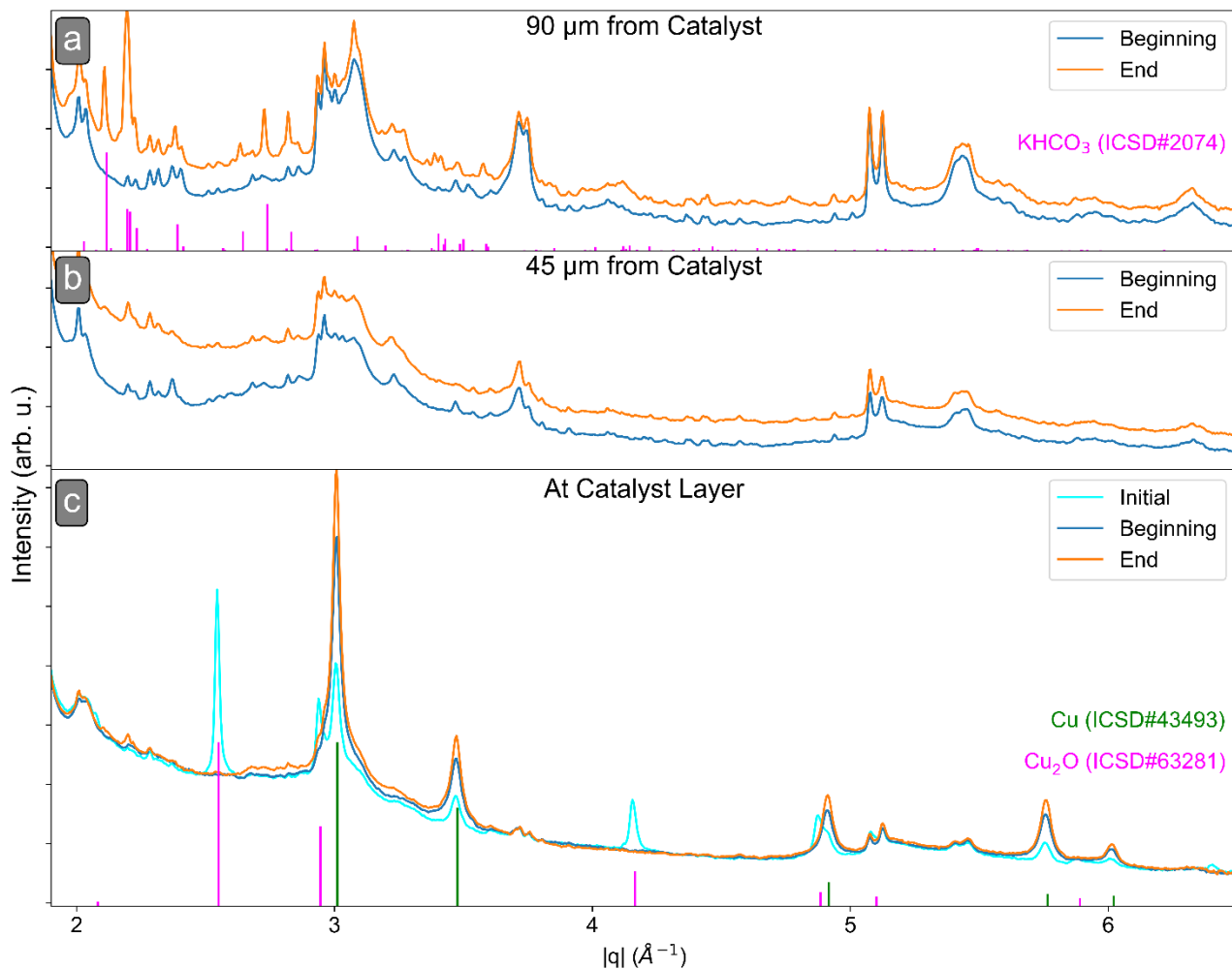

Figure 4 The figure shows patterns obtained from three different positions in the GDE at the beginning and towards the end of a 2.5 h experiment at 200 mA cm^{-2}. Subplot (c) shows patterns obtained at the catalyst layer position. The initial pattern contains both signs of Cu and Cu$_2$O, but the oxide phase disappears fast. In (b) obtained approximately 45 μm from the catalyst layer towards the cathode flowfield not much change can be seen except an increase in the background at low q caused by electrolyte flooding the GDE. Plot (a) shows a similar increase in the background, but also the presence of a KHCO$_3$ phase. Together the various patterns demonstrate how the cell can be used to identify changes inside a GDE.

2.5. Peak splitting and broadening

When scanning along the flow channels, we observed a set of split peaks from the graphite flowfield. The split occurs because the two ends are distanced differently from the detector, the so-called parallax effect (Figure 3b). The same effect is expected to occur with other elements of the cell, e.g. the catalyst layer, but here it will be seen as a peak broadening as the scattering occurs from a continuous film instead of the separated flowfield edges. This is one of the limitations of the cell that one should be aware of, but this can be accounted for during the post-processing of the data[11] and including this effect during the calibration of instrumental parameters.

2.6. Diffraction Tomography

We tested the cell to be used in a diffraction tomography experiment and found it highly suitable for the purpose. An example can be seen in Figure 3a and Figure 5. In such characterization, the pencil beam is scanned along the cell at different azimuthal angles, allowing reconstruction of the full diffraction pattern for each real-space voxel.[12–14] The circular geometry and relatively small width of the cell speeds the measurement process and it possible to obtain an acceptable resolution (in this case 69.5 μm but in principle down to the size of the X-ray beam) with a reasonable acquisition time (about 20 min per slice in this case, with increased time for increased resolution). However, we do in some cases observe damage to the center of the membrane after the tomography scans. While this can limit the tomography possibilities to an extent, carefully selected experimental conditions with respect to the total X-ray dose can mitigate this issue.
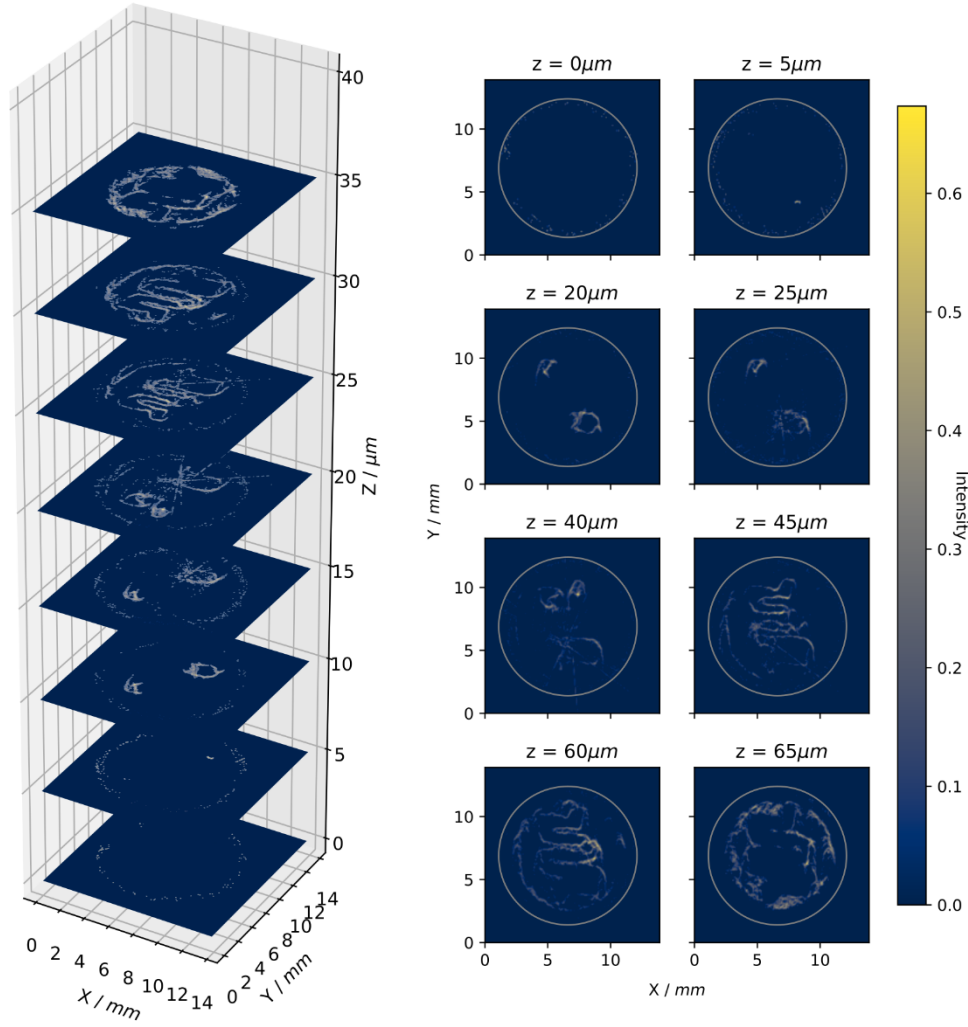
Figure 5. XRD-CT scan of the MEA's Cu catalyst layer before CO₂RR has taken place. The plotted intensity correspond to the surface oxide (Cu₂O) XRD peak (111), integrated in the range of q = 2.49 Å⁻¹ and q = 2.59 Å⁻¹. The dimensions of one voxel is 69.5μm and the dimensions of one slice is 200 x 200 voxels (13.9 x 13.9 mm²). The protrusion of the catalyst layer into the flowfield is clearly detected.
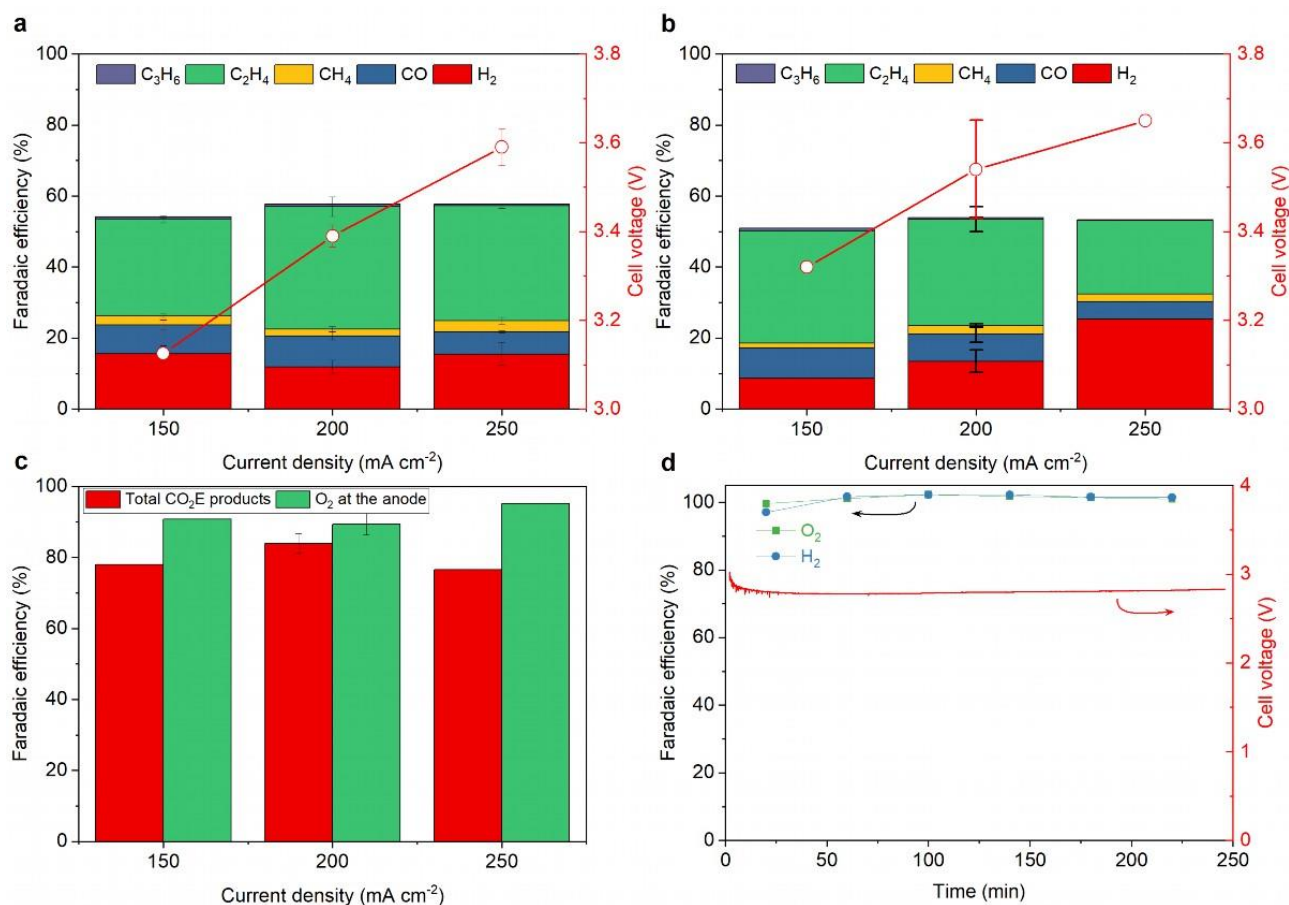
Figure 6. Comparison of electrocatalytic performance in terms of FE of gaseous cathodic products and cell potential over sputtered Cu GDEs (150 nm) in a MEA electrolyzer tested separately at two different locations: (a) without X-rays at DTU and (b) with X-rays at ESRF; (c) Comparison of total FE of CO_2RR products versus FE of O_2 at the anode in experiments performed during X-ray irradiation at ESRF; (d) shows an experiment where Ar was used instead of CO_2 showing a non-corroding anode as the H_2 and O_2 FEs are both 100%; The error bars in (a) show the standard deviation of three separate experiments where the 2nd GC injection was used to calculate the FE, while, the error bars in (b and c) for 200 $mA \cdot cm^{-2}$ show the standard deviation of four separate experiments. 150 and 250 $mA \ cm^{-2}$ experiments shown in (b) (at ESRF) were only performed once due to time limitations.

2.7. Electrochemical Testing

In order to test if the electrolyzer can achieve commercially relevant current densities ($\geq$ 200 mA cm^{-2}) for CO_2 reduction, we investigated the electrocatalytic performance of sputtered Cu GDEs at different current densities. Figure 6a shows that our MEA electrolyzer can produce a reasonable level of gaseous CO_2RR products including CO, CH_4, C_2H_4, C_3H_6, and H_2 during the initial stages of testing (data taken after 30 min of operation). We also see no indication that high energy (69 keV) X-ray illumination alters the electrocatalytic performance significantly. Figure 6a and Figure 6b show the cell performance in terms of faradaic efficiencies of gaseous products and cell potentials, with (6a) and without (6b) X-rays, at different current densities with all operating conditions such as catalysts (both cathode and anode GDE), AEM, and electrolyte kept identical. Furthermore, the experiments tested without X-rays were done at the Technical University of Denmark (DTU) whereas the X-ray irradiated experiments were done at the ID31 beamline of the European Synchrotron Radiation Facility (ESRF), demonstrating the reactor system is robust towards practical laboratory variations as well. In both cases in Figure 6a and Figure 6b, the total FE of products does not reach 100%. The explanation is mainly that the data does not include liquid product analysis. Figure 6c shows the total FE of CO_2RR products (red bars) at different current densities, including liquid products collected at the end of the experiment. With liquid product analysis being the total production of a 3 h experiment, and the gas products being the average of the continuous GC injections, the total faradaic efficiency is an estimated average of the entire experiment and we do therefore not expect the data to match 100% perfectly. The fact that the total FE gets to around 80% and not higher shows that there is still a significant fraction of the current not accounted for.

To account for the missing charge, we calculated the FE of oxygen (O_2) at the anode because if part of the CO_2RR products crosses the membrane and gets oxidized at the anode then the O_2 faradaic efficiency should also decrease. If we assume full anodic oxidation to CO_2, then there would be a one-to-one relationship between unaccounted faradaic efficiency at the cathode and non-O_2 evolution faradaic efficiency at the anode. This principle also assumes a non-corroding anode, which we show to be the case in Figure 6d where Ar was used instead of CO_2 so the only cathode reaction was HER. Here the faradic efficiencies of both H_2 and O_2 are 100%. Since the experiments with X-rays appeared to show the most substantial unaccounted for products, we analyzed the anodic O_2 evolution faradaic efficiency of these experiments. Despite Figure 6c confirming our hypothesis that O_2 faradaic efficiency at the anode does not reach 100% (and thus CO_2RR products are being oxidized) when comparing this to the total faradaic efficiency of CO_2E products as in Figure 6c, there is still a missing 5 to 15% FE. Evaporated liquid products (e.g. ethanol) were not analyzed at either the cathode or anode, which are potential sources for the missing faradaic efficiency.

3. Conclusion

We have presented a design for an electrolysis cell suitable for both water and CO_2 electrolysis with a geometric area large enough to be comparable to other cells, and with a design that allows for various X-ray diffraction and scattering techniques including tomography. The cell design has shown high repeatability in the electrochemical measurements, manageable X-ray background at high energies, and sufficiently easy assembly. The modular design with interchangeable flowplates of different materials makes the cell versatile and suitable for studying various electrochemical processes in MEAs at high current densities.

4. Methods

4.1. MEA setup and electrochemical measurements

For CO_2 electrolysis, a dry CO_2 gas (5N) was fed to the cathode flow-field at 30 sccm using a mass flow controller (Vöegtlin red-y smart series), and 60 ml of 0.1 M $KHCO_3$ anolyte was circulated at the anode using a digitally controlled diaphragm pump (KNF NF1.5TTDCB-4) set at 25% of its maximum speed (which roughly corresponds to 7.5 ml min^{-1}). For the cathode, a 150 nm layer of 6N sputtered Cu was deposited onto Sigracet 39 BB (Fuelcell Store), while, for the anode, a commercial IrO_2-based GDE (from Dioxide Materials, USA) was utilized. In all the experiments, an anion exchange membrane (Sustainion X37-50, Dioxide Materials, USA) activated in 1 M KOH solution and later kept in deionized water was used. All electrochemical experiments were performed in a two-electrode setup at a constant current. Current density of 150, 200, and 250 mA cm^{-2} were applied during galvanostatic measurements using a potentiostat (Biologic SP-300 and SP-240). For selectivity/faradaic efficiency calculations, the gaseous products formed at the cathode (and pre-washed into a deionized water chamber) were injected into an online GC (Agillent 6890A) equipped with a flamed ionization detector with a methanizer and a thermal conductivity detector for the detection of CO, CH_4, C_2H_4, C_3H_6, and H_2, respectively. High-purity argon (5N, Linde Denmark) was used as the carrier gas. The liquid products both collected at the cathode and the anode were detected using a liquid chromatograph (Agilent 1260 Infinity II) with 0.1 M $KHCO_3$ as a reference solution and 0.05 M H_2SO_4 as the internal solvent.

5. Acknowlegement

6. References

1.   Nitopi, S. *et al.* Progress and Perspectives of Electrochemical CO 2 Reduction on Copper in Aqueous Electrolyte. *Chem. Rev.* **119**, 7610–7672 (2019).

2.   Carmo, M., Fritz, D. L., Mergel, J. & Stolten, D. A comprehensive review on PEM water electrolysis. *Int. J. Hydrogen Energy* **38**, 4901–4934 (2013).

3.   Lu, Q. & Jiao, F. Electrochemical CO2 reduction: Electrocatalyst, reaction mechanism, and process engineering. *Nano Energy* **29**, 439–456 (2016).

4.   Weng, L. C., Bell, A. T. & Weber, A. Z. Towards membrane-electrode assembly systems for CO2 reduction: A modeling study. *Energy Environ. Sci.* **12**, 1950–1968 (2019).

5.   Ge, L. *et al.* Electrochemical CO2 reduction in membrane-electrode assemblies. *Chem* vol. 8 663–692 (2022).

6.   Lees, E. W., Mowbray, B. A. W. W., Parlane, F. G. L. L. & Berlinguette, C. P. Gas

diffusion electrodes and membranes for CO2 reduction electrolysers. *Nat. Rev. Mater.* **7**, 55–64 (2022).

7.   Farmand, M. *et al.* Electrochemical flow cell enabling operando probing of electrocatalyst surfaces by X-ray spectroscopy and diffraction. *Phys. Chem. Chem. Phys.* **21**, 5402–5408 (2019).

8.   Hoffmann, H. *et al.* Development of a Modular Operando Cell for X-ray Imaging of Strongly Absorbing Silver-Based Gas Diffusion Electrodes. *J. Electrochem. Soc.* **169**, 044508 (2022).

9.   Olesen, A. C., Rømer, C. & Kær, S. K. A numerical study of the gas-liquid, two-phase flow maldistribution in the anode of a high pressure PEM water electrolysis cell. *Int. J. Hydrogen Energy* **41**, 52–68 (2016).

10.   Moss, A. B. *et al.* In Operando investigations of oscillatory water and carbonate effects in MEA-based CO2 electrolysis devices. *ChemRxiv* https://chemrxiv.org/engage/chemrxiv/article-details/634e8e6933997208578f58c9 (2022) doi:10.26434/chemrxiv-2022-54ccs.

11.   Vamvakeros, A. *et al.* DLSR: A solution to the parallax artefact in X-ray diffraction computed tomography data. *J. Appl. Crystallogr.* **53**, 1531–1541 (2020).

12.   Harding, G., Kosanetzky, J. & Neitzel, U. X-ray diffraction computed tomography. *Med. Phys.* **14**, 515–525 (1987).

13.   Kleuker, U., Suortti, P., Weyrich, W. & Spanne, P. Feasibility study of x-ray diffraction computed tomography for medical imaging. *Phys. Med. Biol.* **43**, 2911 (1998).

14.   Bleuet, P. *et al.* Probing the structure of heterogeneous diluted materials by diffraction tomography. *Nat. Mater. 2008 76* **7**, 468–472 (2008).